Journal of Materials Chemistry A

RSC Publishing

PAPER

View Article Online
View Journal | View Issue

Cite this: J. Mater. Chem. A, 2013, 1, 8201

Role of mesoporosity in cellulose fibers for paper-based fast electrochemical energy storage†

Xinyi Chen,‡[ab] Hongli Zhu,‡[a] Chanyuan Liu,[ab] Yu-Chen Chen,[a] Nicholas Weadock,[a] Gary Rubloff[ab] and Liangbing Hu*[a]

Received 7th March 2013
Accepted 8th May 2013

DOI: 10.1039/c3ta10972k

www.rsc.org/MaterialsA

Paper, a low-cost and flexible substrate made from cellulose fiber, is explored in this study as a platform for fast electrochemical energy storage devices. Conductivity and Li-storage capabilities are introduced to the paper by functionalization with carbon nanotubes (CNTs) and V_2O_5, respectively. The Li-storage paper cathodes present a remarkably high rate performance due to the high conductivity of CNTs, short Li^+ diffusion length in V_2O_5 nanocrystals, and more importantly the hierarchical porosity in paper for Li^+ transport. The specific capacity of V_2O_5 is as high as 410 mA h g^{-1} at 1 C rate, and retains 116 mA h g^{-1} at a high rate of 100 C in the voltage range of 4.0–2.1 V. To understand the role of mesoporosity in individual cellulose fibers, we created a control structure by intentionally blocking the mesopores in paper with a 20 nm Al_2O_3 coating applied *via* atomic layer deposition (ALD). We found that the V_2O_5 capacity decreases by about 30% at high rates of 5–100 C after blocking, which serves to be the first confirmative evidence of the critical role of mesoporosity in paper fibers for high-rate electrochemical devices.

Introduction

Paper has been used as the main medium to record and propagate information and knowledge for more than 2000 years. In recent years, the incorporation of advanced nanomaterials and nanotechnologies has allowed scientists to dramatically expand the applications of paper to other fields including microfluidics,[1,2] organic electronics,[3–5] solar energy harvesting,[6–11] and electrochemical energy storage.[12–14] The motivation has been very clear – paper is both low-cost and flexible. The price of paper is about 10 cents per m^2, orders of magnitude cheaper than plastics, glass, metal foil, silicon, and other traditional substrates. In addition, paper is environmentally friendly as it is recyclable and produced from renewable raw materials.

Paper is produced from a dilute suspension of cellulose fibers which is first dewatered, then filtered, pressed, and heated to give the final product. Both the raw materials and the production process give paper a hierarchical porosity and rough surface.[15,16] This porosity has been considered detrimental to some device applications. Materials printed on paper will have a lower conductivity than on plastics, reducing the performance of organic light-emitting diodes (OLEDs), solar cells, and other devices that require a controlled nanostructure.[5] When attempting to fabricate flexible field-effect transistors (FET) using cellulose fiber paper as a dielectric layer, researchers found that lower porosity is preferred for higher rectification.[17] In other cases, however, the porosity and roughness of paper are advantageous in that they provide good adhesion for printed materials and improve the sensitivity of sensors.[12,18,19]

For energy storage devices, porous paper can be used as a separator membrane[20] and an electrode substrate.[14,21–23] So far, there has been limited focus on porosity engineering in paper-based electrodes and on the relationship between porosity and electrochemical performance. Pores in solid material fall into three categories: micropores (widths smaller than 2 nm), mesopores (widths between 2 and 50 nm), and macropores (widths larger than 50 nm).[24] In this work, we show that the hierarchical porosity of pristine cellulose fiber paper comprises of micrometer-sized macropores between cellulose fibers and mesopores within individual cellulose fibers (2–8 nm). Particularly, we explore the creation of electrochemical energy storage devices on paper-based scaffolds and the relative contribution of the mesopores to the storage through two experimental investigations.

We sequentially functionalize paper with carbon nanotubes (CNTs) for electron conduction and ultrafine V_2O_5 nanoparticles for Li storage (flow 1 in Scheme 1). Due to the high electronic conductivity of CNTs, short Li^+ diffusion length in V_2O_5 nanocrystals, and hierarchical porosity in paper available for Li^+ transport, a high rate performance (*i.e.*, charge/discharge at high power) was successfully achieved on the V_2O_5/CNT/cellulose cathode. In the control experiment represented by flow 2 in Scheme 1, we intentionally blocked the mesopores of

[a]Department of Materials Science and Engineering, University of Maryland, College Park, MD 20742, USA. E-mail: binghu@umd.edu

[b]Institute for Systems Research, University of Maryland, College Park, MD 20742, USA

† Electronic supplementary information (ESI) available. See DOI: 10.1039/c3ta10972k

‡ Equal contribution.

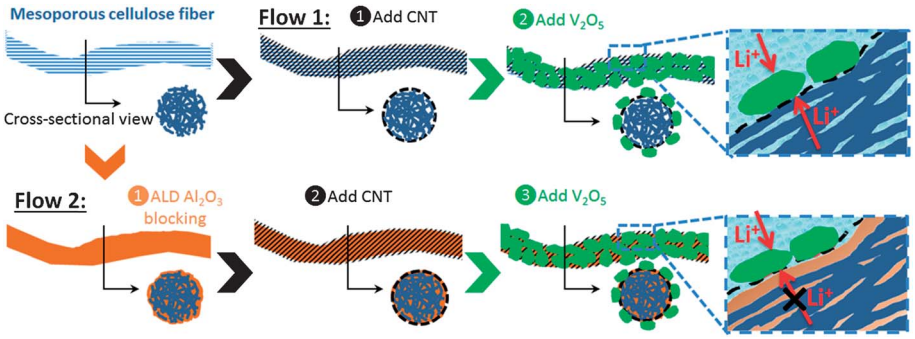

Scheme 1 Two experimental flows to fabricate Li-storage paper cathodes. The general route is to functionalize cellulose fibers with highly conductive CNTs, and then deposit V_2O_5 for Li-ion storage. The major difference between the flows lies in the modification of the cellulose fibers using 20 nm ALD Al_2O_3. We postulate that the mesopores in the cellulose fiber will contribute to the electrochemical capacity by providing extra paths for Li^+ transport during electrochemical charge/discharge. The addition of the ALD Al_2O_3 blocking layer will close off the mesopores, making these pathways unavailable to electrolyte infiltration.

cellulose fiber with 20 nm Al_2O_3 by atomic layer deposition (ALD) before adding CNTs and V_2O_5. This blocked cathode scheme is designated as a V_2O_5/CNT/blocked cellulose cathode. The blocked cathode exhibits a noticeable reduction in rate performance, attributed to the loss of Li^+ transport paths through the cellulose mesopores. Our results indicate that the mesoporosity in the individual cellulose fibers is critical for paper-based electrochemical energy storage devices to achieve high rate performance, *i.e.*, fast energy storage and high power output.

Experimental section

Conductive paper preparation

170 mg of native cellulose fiber disintegrated from southern yellow pine is added to 340 ml distilled (DI) water and stirred with an IKA RW20 Digital at 700 RPM for ~20 min. A uniform fiber suspension was obtained and vacuum filtered through Buchner funnels with fritted discs, forming a wet sheet within 3 min. The sheet is dried in an oven at 100 °C for ~5 min, producing a sheet of paper with a typical thickness of 280 μm. The whole process is water based and additive free. The CNT ink is prepared by adding 10 mg of single wall CNTs (P3 SWCNT from Carbon Solutions) to 10 ml DI water with 1% 4-dodecylbenzenesulfonic acid (SDBS), followed by an 8 minute sonication and centrifugation. The concentration of the CNT ink is 1 mg ml^{-1}. The paper sheet is dipped in the CNT ink for 2–3 min and dried in an oven at 100 °C for 15 min. This procedure is repeated three times to achieve a sheet resistance R_s of 30 ohm per square as measured by a four point probe station. The conductive paper is finally washed with DI water to remove any residual surfactants and dried in a 100 °C oven.

ALD processes

Two ALD processes are involved in this experiment – ALD Al_2O_3 on pristine paper to block the mesopores and ALD V_2O_5 on conductive paper as a Li-storage medium. Both processes were performed in a commercial BENEQ TFS 500 reactor, which has a base pressure of 2 mbar. Al_2O_3 is deposited using trimethyl aluminium [TMA, $Al(CH_3)_3$] and DI water as precursors at 150 °C. The pulse times for the TMA and DI water cycles are intentionally extended from the standard 250 ms to 2 s in order to improve the conformality of Al_2O_3 within the mesopores. The thickness of the ALD Al_2O_3 deposited on a Si wafer after 200 cycles is 20 nm, measured by a SOPRA GES5 spectroscopic ellipsometer. For V_2O_5 deposition we followed the recently reported ozone-based recipe, which produces crystalline V_2O_5 at 170 °C by way of nanocrystal growth and aggregation.[25] Vanadium tri-isopropoxide [VTOP, $VO(OC_3H_7)_3$] is used as the vanadium precursor and kept at 45 °C with a vapor pressure of ~0.29 torr. Ozone generated from a pure O_2 source by an MKS O3MEGA ozone delivery system with a stable concentration of about 18 wt% is used as the oxidant. One ALD cycle for V_2O_5 includes a 0.5 s VTOP pulse, 1 s N_2 purge, 2 s oxidant pulse and 1 s N_2 purge. The V_2O_5 film thickness on Si after 500 cycles was about 10 nm.

Materials characterization

Scanning electron microscopy (SEM) and energy-dispersive X-ray spectroscopy (EDS) characterization is performed with a Hitachi SU-70 SEM. Only the pristine cellulose fibers required a conductive carbon or gold coating. To prepare the samples for cross-sectional observation, the samples were immersed in liquid nitrogen and fractured with tweezers. Special care was taken to avoid sidewall contamination of the cross-sectional area. Transmission electron microscopy (TEM) combined with EDS can provide valuable information on morphology and chemical composition. However, it is difficult to prepare TEM samples with a micrometer thick cellulose fiber substrate. Here, we dropped the CNT solution onto a TEM grid and then placed the TEM grid into an ALD chamber for V_2O_5 deposition. TEM was performed with a JEOL 2100F field emission system with EDS. The paper surface area and pore size were measured with a Micromeritics TriStar II 3020 Porosimeter Test Station. The range of measurable pore sizes is between 17 and 1200 Å. The Brunauer–Emmett–Teller (BET) surface area (calculated from the linear part of the BET plot (P/P_0 = 0.06 – 0.20)) and the Barrett–Joyner–Halenda (BJH) adsorption average pore algorithm are used for evaluating the effect of the ALD Al_2O_3 coating.

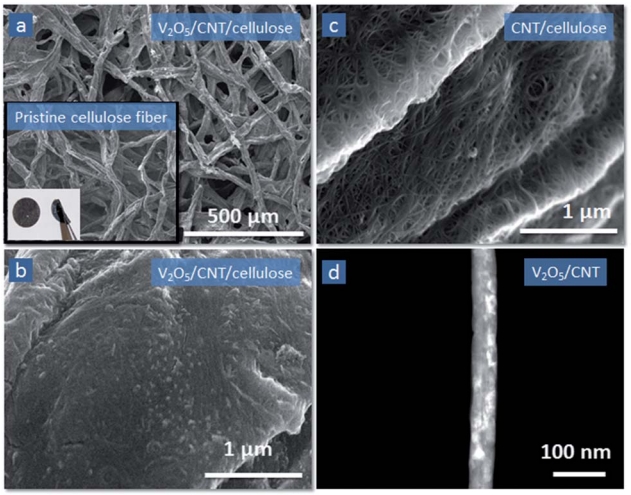

Fig. 1 (a and b) SEM images of cellulose fiber after CNT wrapping and V_2O_5 nanoparticle deposition. These SEM images represent the structure presented in the upper right part of Scheme 1. The inset of (a) shows a pristine cellulose fiber as a reference and a digital photograph of the electrode with and without bending. (c) SEM image of the cellulose fiber after CNT dipping showing high surface coverage of CNTs. (d) Dark field TEM of V_2O_5 deposited CNTs.

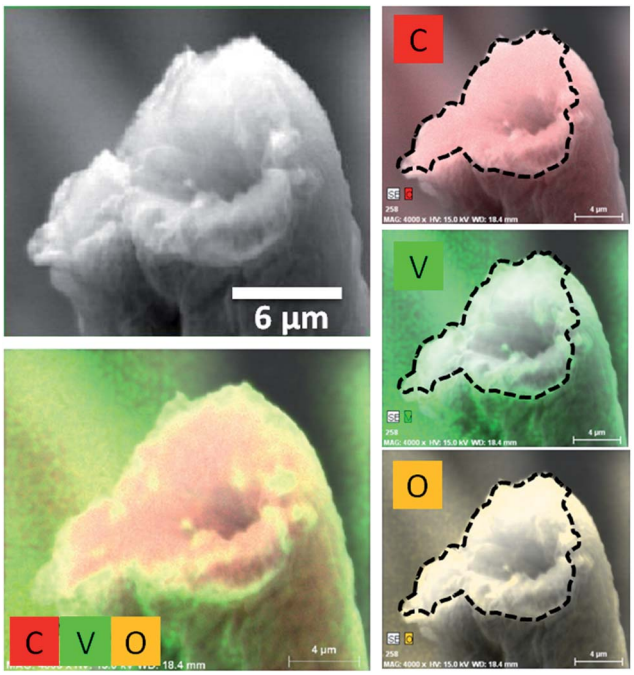

Fig. 2 Cross-sectional SEM and EDS mapping of a single V_2O_5/CNT/cellulose fiber (corresponding to the upper right panel in Scheme 1). The V_2O_5 is present on the outer surface of the CNT/cellulose fiber. The dashed line indicates the V_2O_5 and CNT/cellulose fiber interface.

Li-ion battery assembly and testing

The electrochemical properties of the cellulose-based cathodes are characterized with standard coin cells (CR2032). The samples are punched into disks with a 1/4″ diameter (see digital photograph in the inset of Fig. 1a) and dried overnight in a 100 °C vacuum oven. Coin cells are assembled in an Ar-filled glove box with a Li metal counter electrode and 1 M $LiPF_6$ in ethylene carbonate/diethyl carbonate (EC/DEC, 1 : 1 by volume) electrolyte. The mass of V_2O_5 is determined by weight measurements with a high precision microbalance (Mettler Toledo, XS105 dual Range, 1 μg resolution) before and after V_2O_5 deposition. The V_2O_5 mass loading on the CNT/cellulose fiber is 80 ± 20 μg cm^{-2}. An Arbin BT-2000 multichannel battery test station is used for galvanostatic charging and discharging at various rates. Electrochemical Impedance Spectroscopy (EIS) data are collected from a Bio-logic VMP3 using the EC-lab software.

Synthesis and characterization

The morphology of the cellulose fiber after CNT and V_2O_5 functionalization is shown in Fig. 1a and b at various magnifications. In the low magnification SEM images in the inset of Fig. 1a, the micrometer scale macroporosity can be clearly seen in the pristine cellulose fiber network. The macroporosity remains intact after CNT wrapping and V_2O_5 deposition. Dip coating the cellulose fiber paper in CNT ink adds conductivity, the sheet resistance after coating is 30 ohm per square. Higher magnification images (Fig. 1c) show that the conformal CNT network coats each individual cellulose fiber, contributing to the high conductivity of the paper. The V_2O_5 nanocrystals are deposited using a newly reported ALD process using ozone as the oxidant.[25] For this process, V_2O_5 deposition starts with nucleation at a limited number of sites on a substrate, followed by nanocrystal growth. On Si substrates the nanocrystals form an ~10 nm thick layer after 500 ALD cycles. In a similar way in this work, the CNT network deposited on the cellulose scaffold is expected to produce a low density of hydroxyl groups, leading to an aggregation of V_2O_5 nanocrystals only a few nanometers in size. The high magnification SEM image for V_2O_5/CNT/cellulose (Fig. 1b) shows that the CNT surface is just buried in a new layer and some nanoparticles are visible. TEM also revealed the morphology of V_2O_5 deposition on CNTs. We present here a dark field image of 500 cycle ALD V_2O_5 on a single CNT in Fig. 1d (additional images in Fig. 1S†). The bright dots were confirmed with EDS to be V. One can observe an irregular particle shape of V distribution, consistent with our previous study on the O_3-based ALD V_2O_5 process – evolution with nanocrystal growth.

Cross-section SEM images and EDS element maps of V_2O_5/CNT/cellulose samples are presented in Fig. 2. Within the elemental map, the C signal originates from the cellulose fibers and CNTs, and O signal comes from both cellulose fibers and V_2O_5. The V signal uniquely indicates the V_2O_5 regions. Vanadium is uniformly distributed on the outer surface of the fiber as expected as V_2O_5 deposition is the final step in the sample preparation.

Electrochemical performance

The electrochemical performance of the paper-based electrodes is evaluated in Li half cells using a standard liquid electrolyte and a Li metal anode. Cyclic voltammetry (CV) was used to analyze the charge storage behavior. Fig. 3a shows the typical

cyclic voltammograms for a V_2O_5/CNT/cellulose fiber electrode at various sweep rates. The area under the curves represents the total stored charge which arises from both faradaic and non-faradaic processes. The lithium insertion/extraction in the crystal lattice is represented by the cathodic/anodic peaks, which are not very obvious because we applied relatively fast sweep rates and surface charge storage is significant.

Fig. 3b compares the charge storage capability of CNT/cellulose with and without V_2O_5 deposition in the voltage range of 4.0–2.1 V. With the same current density of 23 μA cm^{-2}, the discharge time of the CNT/cellulose was 360 s, indicating that some charge was stored. Lithiation of CNTs can only occur below 2.0 V,[26] the stored charge for CNT/cellulose, therefore, is attributed to double layer capacitance of the CNTs. Adding V_2O_5 increases the discharge time of the CNT/cellulose to 5030 s, indicating a much larger charge storage capacity. The bare capacity of the CNT/cellulose sample is only ~7% of that with V_2O_5. Furthermore, V_2O_5 should somewhat reduce the available capacity of the CNT since V_2O_5 partially covers the CNT surface. It can be concluded that the charge storage contribution of V_2O_5 in V_2O_5/CNT/cellulose represents at least 93% of the total capacity.

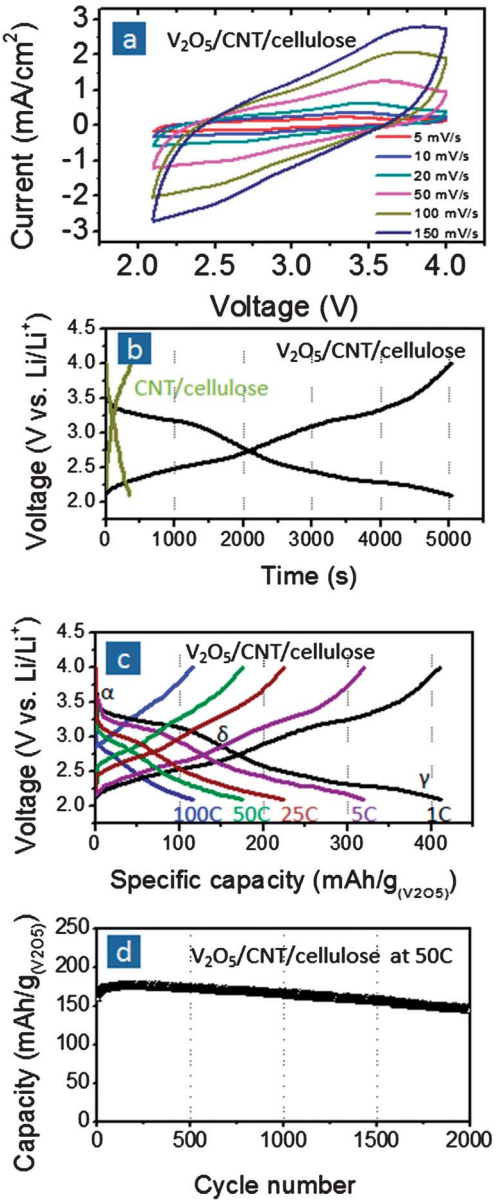

Fig. 3 (a) CV curves of the cells composed of V_2O_5/CNT/cellulose fiber cathodes at scan rates from 5 to 150 mV s^{-1}. (b) Galvanostatic charge/discharge curves of the cells composed of CNT/cellulose fiber cathodes with and without V_2O_5 at a current density of 23 μA cm^{-2}. (c) Galvanostatic charge/discharge curves of the cells with V_2O_5/CNT/cellulose fiber cathodes at current rates ranging from 1 C to 100 C. The phase change of V_2O_5 with respect to lithiation degree is marked on the graph. (d) Cycling performance of the cells with V_2O_5/CNT/cellulose fiber cathodes at 50 C rate.

V_2O_5 is a well-known Li-ion battery cathode material that offers high specific capacity, fast lithiation, and high safety.[27–30] The high specific capacity of V_2O_5 is due to the high oxidation state and unique layered structure that allows two or three Li to intercalate into each V_2O_5 unit. The corresponding theoretical capacities of these two oxidation states are 294 mA h g^{-1} at 4.0–2.1 V and 441 mA h g^{-1} at 4.0–1.5 V, respectively.[31] Three Li intercalation into V_2O_5 has been reported to cause poor cycling stability,[32,33] we therefore limited the voltage range to the two Li intercalation range 4.0–2.1 V to balance capacity and cycling performance. The galvanostatic charge/discharge curves of the V_2O_5/CNT/cellulose cathodes at various C rates are presented in Fig. 3c. A rate of n C corresponds to a current density of 294 × n mA g^{-1}, or an expected full charge or discharge cycle in 1/n hours. Two voltage plateaus are observed on both the discharge and charge curves, representing the characteristic phase transformation of α–δ–γ, as marked in the graph.[31] At 1 C rate, the measured specific capacity of V_2O_5 is 411 mA h g^{-1}, much higher than the theoretical value of 294 mA h g^{-1} for this voltage range. It is not uncommon for nanostructured V_2O_5 materials to achieve a higher capacity than the theoretical value because of a high surface to volume ratio. In a similar V_2O_5/CNT system, Sathiya *et al.* reported an experimental capacity of 850 mA h g^{-1} at 4.0–1.5 V for a theoretical capacity of 441 mA h g^{-1}.[34] High significant surface capacitive charge storage has also been reported in nanosized Mo_2O_3 and TiO_2 systems.[35,36] The extra capacity can be attributed to contributions from surface double layer capacitance and/or excess Li storage capacity at surface defect sites on the electrode material.

The electrochemical performance of the V_2O_5/CNT/cellulose cathodes at higher C rates is plotted in Fig. 3c. At 5 C, 25 C, 50 C, and 100 C, the calculated capacities are 321, 225, 177, and 116 mA h g^{-1}, respectively. This rate performance is among the highest reported for V_2O_5-based high rate cathodes. Chen *et al.* found mesoporous V_2O_5 to have a capacity of 87 mA h g^{-1} at 56 C.[37] Cao *et al.* reported 120 mA h g^{-1} at 70 C from a V_2O_5 nanoelectrode,[38] and the V_2O_5-based high rate cathode reported by Lee *et al.* delivered 102 mA h g^{-1} at 96 C.[33] The excellent rate performance reported here – comparable or better than the others – can be attributed to three unique features in our cathode samples. The first is the high electronic conductivity of the CNT coated paper (30 Ω $\square^{-1}$), allowing for fast electron transport to V_2O_5. Second, the thin V_2O_5 nanocrystal layer significantly reduces the Li^+ diffusion time. McGraw *et al.*

reported the Li diffusivity D in crystalline V_2O_5 over the $2Li/V_2O_5$ voltage range as from 5×10^{-14} to 2×10^{-12} cm^2 s^{-1}.[39] If we take an intermediate value of 1×10^{-13} cm^2 s^{-1}, the kinetic equation $\tau = L^2/2D$ implies a Li diffusion time in a 10 nm film of 5 seconds (corresponding to 720 C). Most importantly, the paper-based electrode scaffold features a hierarchical porous structure, which is well suited for rapid Li^+ transport through the liquid electrolyte to V_2O_5.

The mass ratio of V_2O_5 over the total electrode is about 5% when deposited with 500 ALD cycles. The mass ratio of active material can be increased to 10% with 1000 cycles of ALD V_2O_5. There exists a trade off between the active material loading and rate performance. The cathode with 10% V_2O_5 loading showed similar capacities as the 5% sample at 1 C and 5 C, but noticeable lower capacities at higher C rates of 25 C, 50 C and 100 C (see Fig. 1S†). This can be understood by the fact that Li diffusion in thicker films requires more time.

To estimate the device level performance, we assume that the cathode mass is about 40% of the total device and the energy-power data are presented in the Ragone plot to compare with traditional electrochemical devices (see Fig. 2S†). Although the energy density is lower than that of Li-ion batteries, the achievable power density is much higher (in the scope of capacitors) because of the ultra-high rate performance from the paper-based electrodes. The cycling performance of the V_2O_5/CNT/cellulose cathodes is presented in Fig. 3d. The paper-based cathodes were cycled 2000 times with an initial capacity of 159 mA h g^{-1} and a retained capacity of 146 mA h g^{-1}. The decay of capacity for each cycle is only 0.004%. With the benefits of high power density and excellent cycling performance, the paper electrodes have many promising applications, primarily but not limited to flexible energy storage devices and stationary energy storage.

Role of mesoporosity

Computational modeling has indicated that ion depletion near the electrolyte–electrode interface during electrochemical cycling will limit battery performance.[40] Experimentally, the porosity engineering in electrochemical energy storage nanomaterial electrodes has been studied in several material systems. Rinzler *et al.* reported that by creating macroporosity in the CNT/RuO_2 supercapacitor electrode system, the specific capacitance nearly doubles.[41] In the development of Au electrodes for supercapacitors, Robinson *et al.* found that pores on the order of several hundred nanometers are favored for ion transport. Incorporating these pores achieves a high power density without sacrificing energy density.[42] Similar advances in macroporosity engineering have been made with regards to graphene frameworks for high energy and high power supercapacitors.[43] Introducing macroporosity into electrodes improves ion transport, alleviates ion depletion, and increases the charge/discharge rate; properties desired for high power devices. Macroporosity exists in our composite cathodes between the cellulose fibers as an artifact of the paper fabrication process. We regard the porosity as a major contribution to the high rate performance we observe.

The effect of fiber mesoporosity on the electrochemical performance is investigated by comparing the performance of the as-prepared samples with ones designed to block the mesopores while maintaining macroporosity. Traditional porosity engineering methods, *i.e.*, coating or laminating with polyethylene (PE), polypropylene (PP), PET, wax or other additives will only block the macropores. Instead, we utilize an ALD coating of Al_2O_3, an electrochemically inert material. ALD is a low temperature growth method that alternates sequentially pulsed precursor doses, creating a self-limiting adsorption/reaction process for each precursor with monolayer precision. This results in superb conformality for demanding nanotopography and high-aspect ratio nanostructures.[44] ALD is therefore employed as a technique to precisely tune the pore size in nanomaterials.[45–47]

We ensure that the ALD precursors reach and deposit on the inner surface of the mesopores by increasing the precursor pulse time by a factor of 8 over what is traditionally used for planar film deposition. Fig. 4 is the SEM image and EDS map of the cross-section of a blocked cellulose fiber after CNT and V_2O_5 functionalization as represented in Scheme 1. The SEM shows

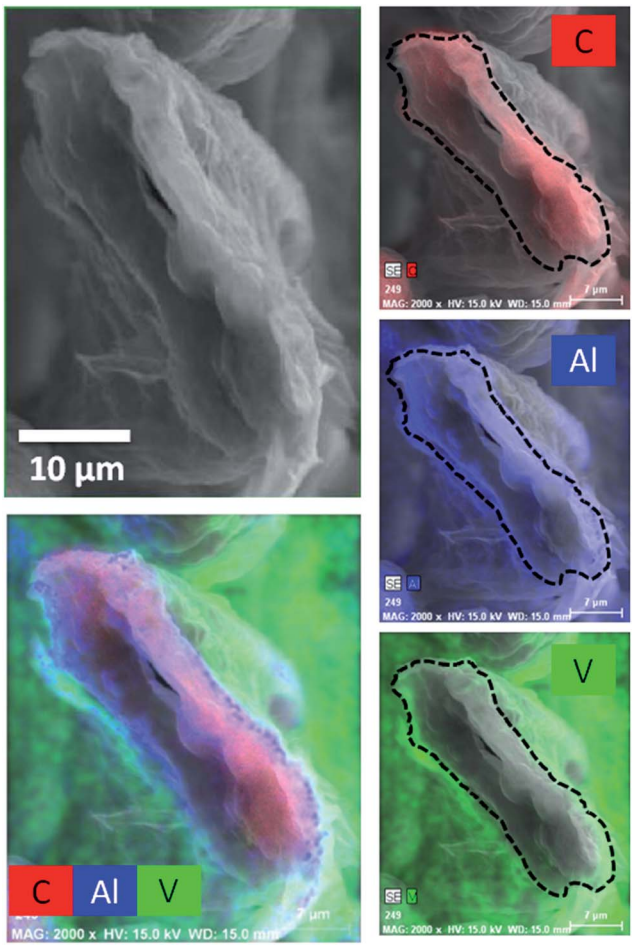

Fig. 4 Cross-sectional SEM and corresponding EDS maps of the V_2O_5/CNT/Al_2O_3 blocked cellulose fiber (bottom right panel in Scheme 1), exhibiting well-defined elemental distributions of C, Al, and V. The dashed line indicates the V_2O_5 and CNT/blocked cellulose fiber interface.

the cross-section to be elongated from top left to bottom right. The EDS overlays on the SEM images clearly show a C–Al–V layered structure, indicating that Al_2O_3 deposited on the cellulose fiber surface prior to CNTs and V_2O_5. This structure corresponds to the one illustrated in the bottom right panel of Scheme 1.

Fig. 5a shows the effect of the ALD Al_2O_3 coating on the pore size distribution of cellulose fibers calculated from BET measurements. For the pristine cellulose fiber, the majority of pore sizes range from 2–8 nm, the mesoporous regime. The addition of the ALD blocking layer causes a distinct shift in the pore size distribution. The majority of the mesopores disappears from the distribution. The few remaining 2–4 nm pores may be due to very small surface cracks generated by the large temperature changes during the porosimetry measurements. The effect of ALD blocking is also strongly reflected by the BET surface area change – the surface area for the pristine mesoporous cellulose fiber is 11.2 $m^2 g^{-1}$ while that for the ALD Al_2O_3 coated cellulose fiber is only 0.07 $m^2 g^{-1}$.

The Al_2O_3 blocking in the cellulose fiber affects the electrochemical properties of the paper-based electrodes. From the EIS data in Fig. 5b, it is apparent that the charge transfer resistance, represented by the diameter of semicircle, is larger in the case of the blocked electrode. We also examined the rate performance of the composite electrodes using pristine mesoporous and ALD-blocked cellulose fibers as substrates. The data presented in Fig. 5c show that the capacity of the unblocked sample is significantly higher than that of the blocked cellulose, especially at higher rates (5–100 C). It is consistent with the observed lower charge transfer resistance in EIS for the unblocked electrode sample. For the V_2O_5/CNT/blocked cellulose, the second cycle discharge capacities are 390, 224, 134, 108 and 77 mA h g^{-1} for rates of 1 C, 5 C, 25 C, 50 C, and 100 C, respectively. The capacity ratios of the mesoporous cellulose fiber relative to the blocked cellulose fiber are 1.05 at 1 C, 1.43 at 5 C, 1.68 at 25 C, 1.62 at 50 C, and 1.50 at 100 C (blue square over brown circle in Fig. 5c). The slightly faster decay in capacity at 1 C and 5 C for the blocked fiber sample can be explained from a possibly weaker binding of the CNT/blocked fiber. We propose the following mechanism to explain the capacity difference between blocked and unblocked samples at different rates. The minimal capacity difference at 1 C (low rate in our study) is likely due to the fact that the slow rate allows Li^+ to completely transport to the V_2O_5 surface. At higher rates (*e.g.* 5–100 C), Li^+ intercalation into V_2O_5 benefits from the additional ion transport channels in the mesoporous fiber channels which are blocked by the ALD layer in the control sample. However, at ultra-high rates beyond what we recorded, only the surface double layer capacitance can respond with the current, and we expect to see a similar performance of the mesoporous fiber electrode and the blocked fiber electrode. This explains the decreased capacity difference when passing a peak value at 25 C. We conclude that ion transport is a dominant factor for achievable capacity at 5–100 C, and the mesoporosity inside the cellulose fiber significantly enhances ion transport to the active material to achieve higher capacity values.

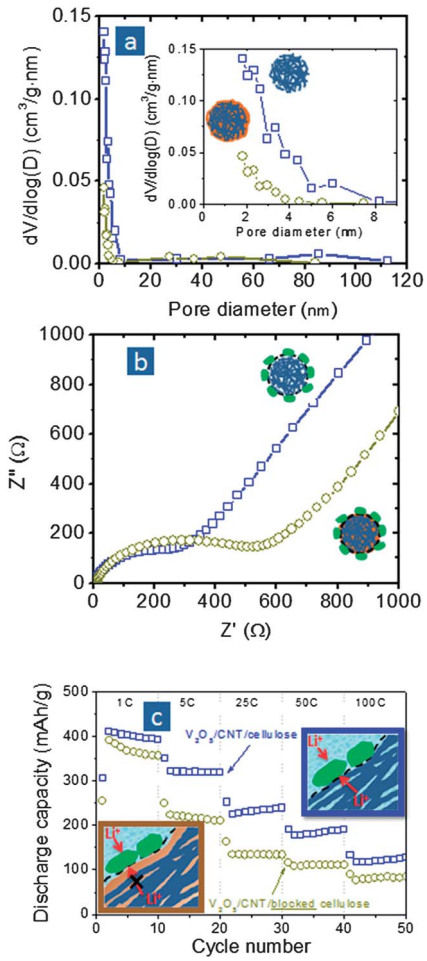

Fig. 5 (a) Pore size distribution of the cellulose fiber with (circles) and without (squares) the 20 nm ALD Al_2O_3 coating. *V* refers to pore volume and *D* pore diameter. (b) EIS curves and (c) rate performance profiles of the Li-storage paper cathode with (circles) and without (squares) the ALD Al_2O_3 coating.

Conclusions

In our effort to understand the mesoporous structure for fast electrochemical energy storage, we fabricated V_2O_5/CNT/cellulose fiber cathodes which exhibit excellent rate performance. Such composite cathodes derive high electronic conductivity from CNTs, short Li^+ diffusion lengths and correspondingly rapid diffusion from nanocrystalline V_2O_5, and fast ion transport from the hierarchical porosity. To quantify the role of mesporosity of the fibers, we compared the results to a control sample in which a 20 nm ALD Al_2O_3 layer was first applied to block the electrolyte access to the mesopores. Porosimetry measurements revealed a significant decrease in the accessible mesoporosity and surface area of the cellulose fibers after the ALD coating. The specific capacity of V_2O_5 at 1 C was not affected by the ALD blocking layer; only at rates above 5 C did the blocking layer cathode experience a ~30% reduction in capacity. From these results we regard ion transport in the electrolyte as the rate-determining mechanism for total achievable capacity. This work clearly indicates that mesopores within a cellulose fiber act as an electrolyte reservoir and

provide extra paths for Li^+ transport. The use of porous, electrochemically inert paper as a substrate sacrifices some volume energy and power density, however it provides efficient utilization of active storage materials at high rates. Our high-rate paper-based cathodes can be applied in flexible storage devices and stationary energy storage technologies to efficiently manage smart grid as well as energy from renewable sources.

Acknowledgements

X. Chen, C. Liu and G. Rubloff are supported by Nanostructures for Electrical Energy Storage (NEES), an Energy Frontier Research Center funded by the U.S. Department of Energy, Office of Science, Office of Basic Energy Sciences under Award Number DESC0001160. L. Hu, a NEES affiliate, and his team H. Zhu and Y. Chen, and N. Weadock are supported by startup funds from the University of Maryland. We also acknowledge the support of the Maryland NanoCenter and its FabLab and NispLab, and Professor Peter Kofinas from Fischell Department of Bioengineering for providing access to a high precision microbalance.

References

1 E. Carrilho, A. W. Martinez and G. M. Whitesides, *Anal. Chem.*, 2009, **81**, 7091–7095.
2 A. W. Martinez, S. T. Phillips and G. M. Whitesides, *Proc. Natl. Acad. Sci. U. S. A.*, 2008, **105**, 19606–19611.
3 F. Eder, H. Klauk, M. Halik, U. Zschieschang, G. Schmid and C. Dehm, *Appl. Phys. Lett.*, 2004, **84**, 2673–2675.
4 R. Martins, I. Ferreira and E. Fortunato, *Phys. Status Solidi*, 2011, **5**, 332–335.
5 D. Tobjork and R. Osterbacka, *Adv. Mater.*, 2011, **23**, 1935–1961.
6 S. I. Cha, Y. Kim, K. H. Hwang, Y. J. Shin, S. H. Seo and D. Y. Lee, *Energy Environ. Sci.*, 2012, **5**, 6071–6075.
7 K. Fan, T. Y. Peng, J. N. Chen, X. H. Zhang and R. J. Li, *J. Mater. Chem.*, 2012, **22**, 16121–16126.
8 S. Roy, R. Bajpai, A. K. Jena, P. Kumar, N. Kulshrestha and D. S. Misra, *Energy Environ. Sci.*, 2012, **5**, 7001–7006.
9 B. Wang and L. L. Kerr, *Sol. Energy Mater. Sol. Cells*, 2011, **95**, 2531–2535.
10 M. C. Barr, J. A. Rowehl, R. R. Lunt, J. J. Xu, A. N. Wang, C. M. Boyce, S. G. Im, V. Bulovic and K. K. Gleason, *Adv. Mater.*, 2011, **23**, 3500–3505.
11 A. Hubler, B. Trnovec, T. Zillger, M. Ali, N. Wetzold, M. Mingebach, A. Wagenpfahl, C. Deibel and V. Dyakonov, *Adv. Energy Mater.*, 2011, **1**, 1018–1022.
12 L. B. Hu, J. W. Choi, Y. Yang, S. Jeong, F. La Mantia, L. F. Cui and Y. Cui, *Proc. Natl. Acad. Sci. U. S. A.*, 2009, **106**, 21490–21494.
13 L. Nyholm, G. Nystrom, A. Mihranyan and M. Stromme, *Adv. Mater.*, 2011, **23**, 3751–3769.
14 V. L. Pushparaj, M. M. Shaijumon, A. Kumar, S. Murugesan, L. Ci, R. Vajtai, R. J. Linhardt, O. Nalamasu and P. M. Ajayan, *Proc. Natl. Acad. Sci. U. S. A.*, 2007, **104**, 13574–13577.
15 R. J. Moon, A. Martini, J. Nairn, J. Simonsen and J. Youngblood, *Chem. Soc. Rev.*, 2011, **40**, 3941–3994.
16 S. Polarz, B. Smarsly and J. H. Schattka, *Chem. Mater.*, 2002, **14**, 2940–2945.
17 E. Fortunato, N. Correia, P. Barquinha, L. Pereira, G. Goncalves and R. Martins, *IEEE Electron Device Lett.*, 2008, **29**, 988–990.
18 F. G. Souza, G. E. Oliveira, T. Anzai, P. Richa, T. Cosme, M. Nele, C. H. M. Rodrigues, B. G. Soares and J. C. Pinto, *Macromol. Mater. Eng.*, 2009, **294**, 739–748.
19 J. Huang, H. Zhu, Y. Chen, C. Preston, K. Rohrbach, J. Cumings and L. Hu, *ACS Nano*, 2013, **7**, 2106–2113.
20 S. J. Chun, E. S. Choi, E. H. Lee, J. H. Kim and S. Y. Lee, *J. Mater. Chem.*, 2012, **22**, 16618–16626.
21 L. B. Hu, H. Wu, F. La Mantia, Y. A. Yang and Y. Cui, *ACS Nano*, 2010, **4**, 5843–5848.
22 G. Nystrom, A. Razaq, M. Stromme, L. Nyholm and A. Mihranyan, *Nano Lett.*, 2009, **9**, 3635–3639.
23 L. Jabbour, M. Destro, C. Gerbaldi, D. Chaussy, N. Penazzi and D. Beneventi, *J. Mater. Chem.*, 2012, **22**, 3227–3233.
24 J. Rouquerol, D. Avnir, C. W. Fairbridge, D. H. Everett, J. H. Haynes, N. Pernicone, J. D. F. Ramsay, K. S. W. Sing and K. K. Unger, *Pure Appl. Chem.*, 1994, **66**, 1739–1758.
25 X. Y. Chen, E. Pomerantseva, P. Banerjee, K. Gregorczyk, R. Ghodssi and G. Rubloff, *Chem. Mater.*, 2012, **24**, 1255–1261.
26 Y. Liu, H. Zheng, X. H. Liu, S. Huang, T. Zhu, J. W. Wang, A. Kushima, N. S. Hudak, X. Huang, S. L. Zhang, S. X. Mao, X. F. Qian, J. Li and J. Y. Huang, *ACS Nano*, 2011, **5**, 7245–7253.
27 J. M. Tarascon and M. Armand, *Nature*, 2001, **414**, 359–367.
28 C. K. Chan, H. L. Peng, R. D. Twesten, K. Jarausch, X. F. Zhang and Y. Cui, *Nano Lett.*, 2007, **7**, 490–495.
29 Y. Wang and G. Z. Cao, *Adv. Mater.*, 2008, **20**, 2251–2269.
30 X. Chen, E. Pomerantseva, K. Gregorczyk, R. Ghodssi and G. Rubloff, *RSC Adv.*, 2013, **3**, 4294–4302.
31 M. S. Whittingham, Y. N. Song, S. Lutta, P. Y. Zavalij and N. A. Chernova, *J. Mater. Chem.*, 2005, **15**, 3362–3379.
32 X. Y. Chen, H. L. Zhu, Y. C. Chen, Y. Y. Shang, A. Y. Cao, L. B. Hu and G. W. Rubloff, *ACS Nano*, 2012, **6**, 7948–7955.
33 J. A. Yan, A. Sumboja, E. Khoo and P. S. Lee, *Adv. Mater.*, 2011, **23**, 746.
34 M. Sathiya, A. S. Prakash, K. Ramesha, J. M. Tarascon and A. K. Shukla, *J. Am. Chem. Soc.*, 2011, **133**, 16291–16299.
35 J. Wang, J. Polleux, J. Lim and B. Dunn, *J. Phys. Chem. C*, 2007, **111**, 14925–14931.
36 T. Brezesinski, J. Wang, S. H. Tolbert and B. Dunn, *Nat. Mater.*, 2010, **9**, 146–151.
37 S. Q. Wang, S. R. Li, Y. Sun, X. Y. Feng and C. H. Chen, *Energy Environ. Sci.*, 2011, **4**, 2854–2857.
38 Y. Y. Liu, M. Clark, Q. F. Zhang, D. M. Yu, D. W. Liu, J. Liu and G. Z. Cao, *Adv. Energy Mater.*, 2011, **1**, 194–202.
39 J. M. McGraw, C. S. Bahn, P. A. Parilla, J. D. Perkins, D. W. Readey and D. S. Ginley, *Electrochim. Acta*, 1999, **45**, 187–196.
40 V. Zadin, D. Brandell, H. Kasemagi, A. Aabloo and J. O. Thomas, *Solid State Ionics*, 2011, **192**, 279–283.

41 R. N. Das, B. Liu, J. R. Reynolds and A. G. Rinzler, *Nano Lett.*, 2009, **9**, 677–683.
42 W. S. Chae, D. Van Gough, S. K. Ham, D. B. Robinson and P. V. Braun, *ACS Appl. Mater. Interfaces*, 2012, **4**, 3973–3979.
43 B. G. Choi, M. Yang, W. H. Hong, J. W. Choi and Y. S. Huh, *ACS Nano*, 2012, **6**, 4020–4028.
44 S. M. George, *Chem. Rev.*, 2010, **110**, 111–131.
45 J. Dendooven, B. Goris, K. Devloo-Casier, E. Levrau, E. Biermans, M. R. Baklanov, K. F. Ludwig, P. Van der Voort, S. Bals and C. Detavernier, *Chem. Mater.*, 2012, **24**, 1992–1994.
46 C. Detavernier, J. Dendooven, S. P. Sree, K. F. Ludwig and J. A. Martens, *Chem. Soc. Rev.*, 2011, **40**, 5242–5253.
47 F. B. Li, L. Li, X. Z. Liao and Y. Wang, *J. Membr. Sci.*, 2011, **385**, 1–9.